Three-dimensional MHD simulation of a flux rope driven CME

Ward B. Manchester IV, Tamas I. Gombosi, Ilia Roussev, Darren L. De Zeeuw,
I. V. Sokolov, Kenneth G. Powell, and Gábor Tóth[1]
Center for Space Environment Modeling, University of Michigan, Ann Arbor, Michigan, USA

Merav Opher
Jet Propulsion Laboratory, California Institute of Technology, Pasadena, California, USA

Received 6 September 2002; revised 21 August 2003; accepted 11 September 2003; published 6 January 2004.

[1] We present a three-dimensional (3-D) numerical ideal magnetohydrodynamics (MHD) model, describing the time-dependent expulsion of plasma and magnetic flux from the solar corona that resembles a coronal mass ejection (CME). We begin by developing a global steady-state model of the corona and solar wind that gives a reasonable description of the solar wind conditions near solar minimum. The model magnetic field possesses high-latitude coronal holes and closed field lines at low latitudes in the form of a helmet streamer belt with a current sheet at the solar equator. We further reproduce the fast and slow speed solar wind at high and low latitudes, respectively. Within this steady-state heliospheric model, conditions for a CME are created by superimposing the magnetic field and plasma density of the 3-D Gibson-Low flux rope inside the coronal streamer belt. The CME is launched by initial force imbalance within the flux rope resulting in its rapid acceleration to a speed of over 1000 km/s and then decelerates, asymptotically approaching a final speed near 600 km/s. The CME is characterized by the bulk expulsion of $\sim 10^{16}$ g of plasma from the corona with a maximum of $\sim 5 \times 10^{31}$ ergs of kinetic energy. This energy is derived from the free magnetic energy associated with the cross-field currents, which is released as the flux rope expands. The dynamics of the CME are followed as it interacts with the bimodal solar wind. We also present synthetic white-light coronagraph images of the model CME, which show a two-part structure that can be compared with coronagraph observations of CMEs. *INDEX TERMS:* 7513 Solar Physics, Astrophysics, and Astronomy: Coronal mass ejections; 7524 Solar Physics, Astrophysics, and Astronomy: Magnetic fields; 7509 Solar Physics, Astrophysics, and Astronomy: Corona; 7531 Solar Physics, Astrophysics, and Astronomy: Prominence eruptions; *KEYWORDS:* magnetohydrodynamics, Sun, coronal mass ejection

Citation: Manchester, W. B., IV, T. I. Gombosi, I. Roussev, D. L. De Zeeuw, I. V. Sokolov, K. G. Powell, G. Toth, and M. Opher (2004), Three-dimensional MHD simulation of a flux rope driven CME, *J. Geophys. Res.*, *109*, A01102, doi:10.1029/2002JA009672.

1. Introduction

[2] Coronal mass ejections (CMEs) have traditionally been defined as large-scale expulsions of plasma from the corona seen as bright arcs in coronagraphs that record Thomson scattered light. These events are the most stunning activity of the solar corona in which typically $10^{15}-10^{16}$ g of plasma is hurled into interplanetary space with a kinetic energy of the order 10^{31-32} ergs. Extensive observations with the SMM coronagraph have shown that the majority of CMEs originate from the disruption of large-scale coronal structures known as helmet streamers [*Hundhausen*, 1988, 1993]. Helmet streamers are arcade-like structures commonly found in coronagraph images that possess a three-part structure composed of a high-density shell covering a low-density cavity, at the base of which lies a filament. That CMEs originate from helmet streamers is strongly suggested by the appearance of many CMEs possessing a dense bright leading shell with a cavity containing a bright core, which can be interpreted as the corresponding three-part structure of the of the preevent helmet streamer as shown by *Hundhausen* [1999] and *Howard et al.* [1997]. It is now believed that the breakup of helmet streamers may result from a loss of equilibrium following a slow, nearly quasi-static evolution [*Low*, 1983]. A slow growth followed by eruption is consistent with the observations of the swelling and brightening of large coronal helmet streamers several days before they produce CMEs [*Hundhausen*, 1993].

[3] Central to understanding the dynamics of CMEs is the nature of the preevent magnetic field, about which much can be inferred from both theory and observations. For a helmet streamer to be in static equilibrium, the underlying

[1] Also at Department of Atomic Physics, Eotvos University, Budapest, Hungary.

0148-0227/04/2002JA009672

magnetic field must be in a closed configuration to confine the dense plasma that would otherwise be carried out with the solar wind. Observations show that the photospheric magnetic field associated with helmet streamers is in a bipolar configuration where opposite polarities are largely separated by a neutral line. Furthermore, in the corona, X-ray loops are clearly found to coincide with the helmet streamers, indicating a dominant loop-type magnetic field configuration [*Sterling and Hudson*, 1997]. A significant feature of the field configurations associated with CMEs is magnetic shear, which is observed at the photosphere with vector magnetograms [*Wang and Sheeley*, 1994] and is strongly suggested in the corona by the presence of X-ray sigmoids [*Moore et al.*, 2001]. Thus the magnetic field configuration of preevent helmet streamers is a sheared arcade possibly containing a flux rope as suggested by *Low* [1994] and *Low and Hundhausen* [1995] coinciding with the plasma cavity. It is believed that CMEs are the result of a global magnetohydrodynamic (MHD) process and represent a significant restructuring of the global coronal magnetic field [*Low*, 1996].

[4] Observational limitations combined with the complexity of CME structure and dynamics have lead to a diverse number of models that capture various aspects of the eruption process. Early theories of initiation suggested that thermal pressure associated with solar flares was the driving mechanism [*Dryer et al.*, 1979]. However, this model fell from favor when observations revealed that flares often occur after CME initiation [*Hundhausen*, 1999]. More recent observations have shown that soft X-ray emissions increase with CME initiation, particularly for fast CMEs [*Zhang et al.*, 2002]. It is now believed that only the solar magnetic field is capable of driving CMEs [*Forbes*, 2000]. Nearly all magnetic-driven models of CMEs have employed preevent coronal magnetic fields of two distinct topologies: sheared magnetic arcades or magnetic flux ropes often contained within an arcade. Examples of flux rope models include *Mouschovias and Poland* [1978], *Chen* [1996], *Wu and Guo* [1997], *Wu et al.* [1999], and *Wu et al.* [2000]. CME models with simple arcade configurations include *Wolfson* [1982], *Mikić et al.* [1988], *Steinolfson* [1991], *Choe and Lee* [1996], *Mikić and Linker* [1994], and *Linker and Mikić* [1995]. Flux ropes offer some advantages over arcades in that they offer a structure that more naturally supports prominence material and explains the cavity and core of the three part density structure commonly observed in CMEs. In addition, flux ropes detached from the solar surface can store free magnetic energy capable of powering CMEs [*Low*, 2001]. However, while flux ropes may be theoretically appealing there is still little direct observational evidence supporting the existence of preevent coronal flux ropes while arcade type structures are commonly observed in the corona before and after CMEs.

[5] Regardless of topology, the preevent magnetic fields are usually taken to be either potential or force-free. The potential field has zero free energy while the force-free field has been shown by *Aly* [1991] and *Sturrock* [1991] to possess less energy than the open state, greatly limiting its ability to erupt. To induce an eruption from such magnetic states, several mechanisms have been invoked. In the case of flux ropes, the injection of azimuthal magnetic flux has been used to drive eruptions as in the works of *Chen* [1996] and *Wu et al.* [1999]. Localized magnetic reconnection has been selectively introduced to sever field lines and relieve magnetic tension to allow a portion of the system (typically a flux rope) to expand rapidly upwards. Examples of reconnection-driven CME models are those by *Forbes and Priest* [1995], *Lin and Forbes* [2000], and *Chen and Shibata* [2000]. Also, a combination of system driving and magnetic reconnection has been used to model the initiation of CMEs. In the most common example, two-dimensional (2-D) magnetic arcades are made to approach an open state by way of prescribed footpoint motions that shear the magnetic field. Reconnection when applied within the shearing arcade results in eruption [*Steinolfson*, 1991; *Choe and Lee*, 1996; *Linker and Mikić*, 1995]. *Antiochos et al.* [1999] have produced a new variation of this model employing a quadrupole field that allows magnetic reconnection to occur higher in the corona, which removes the unsheared field above a low-lying sheared core.

[6] Only recently have CME models been produced that allow for fully three-dimensional (3-D) spatial variation. *Gibson and Low* [1998] gives an analytical description of the expansion of a flux rope as a CME while *Amari et al.* [2000] perform a numerical MHD simulation of the formation of a flux rope within an arcade and its subsequent eruption. Lately, a numerical model of coronal arcades responding to rotating photospheric flows has been produced by *Tokman and Bellan* [2002]. In this case, the authors find that the evolving magnetic field mimics the three-part structure of CMEs.

[7] The approach we take to modeling CMEs is to start with a system that is initially out of equilibrium and simulate its subsequent time evolution. We begin by numerically forming a steady-state model of the corona along with a bimodal solar wind. The model coronal magnetic field is representative of a solar minimum configuration with open polar field lines and low-latitude closed field lines forming a streamer belt. Having attained this steady-state, we then place a 3-D magnetic flux rope within the streamer belt, which is tied at both ends to the inner boundary. The flux rope we use is taken from a family of 3-D analytical solutions derived by *Gibson and Low* [1998, hereinafter referred to as GL], which provide time-dependent, self-similar MHD models of CMEs. In the case of GL, the flux rope is initially in equilibrium in which radially outward directed Lorentz force is balanced by the weight and pressure of contained plasma. The flux rope then expands as a result of an applied velocity field, which is prescribed so that the flux rope expands in a self-similar fashion resembling a CME. Here, we have superimposed both the magnetic field and density of the GL flux rope onto the steady-state corona. Rather than imparting an initial outward flow, we leave the system at rest but insert the flux rope within the system with reduced mass and insufficient external pressure for the system to be in equilibrium. This configuration allows the system to contain substantial free energy and circumvents the constraint of *Aly* [1991] and *Sturrock* [1991] by virtue of a nonzero cross-field component of the electric current. In the subsequent time evolution of the system, we find that the flux rope expands rapidly, driving a strong shock ahead of it as it is expelled from the corona along with large amounts of plasma mimicking a CME. With our inclusion of this flux rope to a numerical, steady-state model

of the corona and solar wind, we can extend the Gibson Low model to address its limitations such as CME acceleration and interaction with a background solar wind, as well as allowing for magnetic reconnection.

[8] The organization of the paper is as follows. We give a brief description of the conservative form of the equations of MHD and the scheme used to solve them in section 2. Details of the steady-state corona and solar wind are given in section 3, while an outline of the Gibson-Low flux rope is given in section 4. Results of the numerical simulation of the flux rope driven CME are given in section 5, which includes a discussion of the energy budget and velocity profile. In addition, synthetic, Thomson-scattered, white light images of the CME are presented as seen from three different perspectives. Finally, in section 6, we discuss the simulation results and their significance in demonstrating magnetic flux ropes as a possible driver of CMEs.

2. Governing Equations of the MHD Model

[9] In our model of the corona, solar wind, and CME, we assume that the systems are composed of magnetized plasma that behaves as an ideal gas with a polytropic index, $\gamma = 5/3$. The plasma is assumed to have infinite electrical conductivity so that the magnetic field is "frozen" into the plasma. Gravitational forces on the plasma are included but only forces due to the Sun; there is no self-gravitation of the plasma. Finally, volumetric heating of the plasma of a chosen form is assumed to occur in the corona. With these assumptions, the evolution of the system may be modeled by the ideal MHD equations written in conservative form:

$$\frac{\partial \rho}{\partial t} + \nabla \cdot (\rho \boldsymbol{u}) = 0 \tag{1}$$

$$\frac{\partial (\rho \boldsymbol{u})}{\partial t} + \nabla \cdot \left[\rho \boldsymbol{u}\, u + \left(p + \frac{B^2}{8\pi} \right) I - \frac{\boldsymbol{B}\, B}{4\pi} \right] = \rho \boldsymbol{g} \tag{2}$$

$$\frac{\partial \boldsymbol{B}}{\partial t} + \nabla \cdot (\boldsymbol{u}\, B - \boldsymbol{B}\, u) = 0 \tag{3}$$

$$\frac{\partial \varepsilon}{\partial t} + \nabla \cdot \left[\boldsymbol{u} \left(\varepsilon + p + \frac{B^2}{8\pi} \right) - \frac{(\boldsymbol{u} \cdot \boldsymbol{B}) \boldsymbol{B}}{4\pi} \right], = \rho \boldsymbol{g} \cdot \boldsymbol{u} + (\gamma - 1) Q, \tag{4}$$

where ρ is the plasma mass density, $\boldsymbol{u}$ is the plasma velocity, $\boldsymbol{B}$ is the magnetic field, and p is the plasma pressure (sum of the electron and ion pressures). The volumetric heating term, Q, parameterizes the effects of coronal heating as well as heat conduction and radiation transfer (see section 3). The gravitational acceleration is defined as $\boldsymbol{g} = -g(\boldsymbol{r}/r)(R_\odot/r)^2$, where $R_\odot$ is the solar radius and g is the gravitational acceleration at the solar surface. The total energy density, ε, is given by

$$\varepsilon = \frac{\rho u^2}{2} + \frac{p}{\gamma - 1} + \frac{B^2}{8\pi}. \tag{5}$$

This system of eight equations details the transport of mass, momentum, and energy with three equations describing the evolution of the magnetic field given by Faraday's Law assuming infinite electrical conductivity. These equations are then put in dimensionless form, using values of the density and ion-acoustic wave speed from a suitable part of the physical domain (in this case the low corona) in addition to a reference length scale (in this case the solar radius). The dimensionless equations are then solved, using the block-adaptive tree solar wind Roe-type upwind scheme (BATS-R-US) code [*Powell et al.*, 1999; *Groth et al.*, 2000]. This code is designed to run efficiently on massively parallel computers and solves the equations of MHD with the use of block adaptive mesh refinement (AMR). This feature of the grid allows for orders of magnitude variation in numerical resolution within the computational domain. Such resolution is necessary for global coronal models, which strive to resolve structures such as shocks and electric current sheets in a domain that extends to many solar radii.

3. Steady-State Model of the Solar Wind

[10] In order to simulate the time-dependent behavior of a CME propagating from the low corona through the solar wind, a representative MHD model of the steady-state background solar wind is required. With such a model, the evolution of a CME is then formulated as a propagation problem with the initial condition of the corona and solar wind specified by the steady-state solution.

[11] In this section, we describe our steady-state model of the corona and solar wind that is designed to reproduce conditions near solar minimum. The essential features of this model are (1) open magnetic field lines forming coronal holes at high latitude; (2) closed magnetic field lines forming a streamer belt near the Sun at low latitudes; (3) the bimodal nature of the solar wind is reproduced with fast wind over the poles and slow wind at low latitudes. A thin current sheet forms at the tip of the streamer belt and separates opposite directed magnetic flux originating from the two poles. The model is simplified by alignment of the magnetic axis with the z axis so the solution is axisymmetric. Also, solar rotation is neglected since the domain extends only to 32 solar radii. At this distance from the Sun, the azimuthal component of the *Parker* [1963] spiral is negligible. While the magnetic field structure of this steady-state solution is simple, future models will eventually incorporate synoptic magnetogram observations as well as a rotating Sun to form much more realistic magnetic field configurations.

[12] The corona is composed of high-temperature ($T > 10^6$ K), low-density ($\rho \approx 10^{-16}$ gm cm^{-3}) plasma composed primarily of ionized hydrogen. The temperature and pressure of the corona are such that it can not be held in equilibrium by solar gravity or the pressure of the interstellar medium. Consequently, it expands outward at supersonic speeds and in doing so forms the solar wind [*Parker*, 1963]. The fast solar wind originates from coronal holes and is possibly driven to high velocity by additional heating that occurs close to the Sun [cf. *Axford and McKenzie*, 1996]. It is also thought that momentum deposited by Alfven waves may accelerate this component of the wind [cf. *Hollweg et al.*, 1982; *Usmanov et al.*, 2000]. The fast wind lies at heliolatitudes >30° at solar minimum and has an average velocity of the approximately 750 km s^{-1}. The slow wind

by contrast is confined close to the global heliospheric current sheet, which lies near the equator at solar minimum. This component of the wind is highly variable with speeds that lie between 300 and 450 km s^{-1}. The source of the slow wind may be highly expanded plasma traveling down magnetic flux tubes that originate near coronal hole boundaries. It has also been suggested that opening of closed flux tubes by interchange reconnection with open flux may release plasma to form the slow solar wind [*Fisk et al.*, 1999].

[13] The steady-state model of the corona and solar wind described here was first developed by *Groth et al.* [2000]. However, we have made significant modifications to the original steady-state model to suit our purposes. First, our simulation is performed in the inertial frame rather than the corotating frame. Second, the magnetic axis is aligned with the z axis in our model rather than having a tilted intrinsic magnetic field topology. Third, we have slightly modified the inner boundary condition to allow for the flux rope to be line-tied to the coronal surface. Finally, our model of the solar wind only extends to $32R_\odot$ compared to $224R_\odot$ of the original model with a different numerical grid and with the absence of solar rotation. In all other ways, our steady-state model is identical to *Groth et al.* [2000], of which we briefly outline here.

[14] The steady-state numerical model is made with the assumption that the base of the corona is at the inner boundary and acts as a reservoir of hot plasma with an embedded magnetic field. The plasma temperature (the sum of the ion and electron temperatures) is taken to be $T_s = T_p + T_e = 2.85 \times 10^6$ K with $T_p/T_e \sim 2$. For the remainder of the text, we will refer only to the plasma temperature, T_s. The plasma density is taken to be $\rho = 2.5 \times 10^{-16}$ gm cm^{-3}. The intrinsic magnetic field at the solar surface, $\boldsymbol{B}_0$, may be written as a multipole expansion of the following form:

$$B_{0k} = 3\frac{M_i r_i}{r^4}\frac{r_k}{r} - \frac{M_k}{r^3} + 7\frac{Q_{ijl} r_i r_j r_l}{r^8}\frac{r_k}{r} - 3\frac{Q_{ijk} r_i r_j}{r^7}, \quad (6)$$

where M_i (i = 1, 2, 3) are the components of the dipole moment vector and Q_{ijk} are the octupole moment tensor components with the octupole aligned with the z axis (there is no quadrupole moment in this model). We have taken the dipole aligned with the z axis so that $M_x = M_y = 0$ and $M_z = b_0$. The dipole and octupole moments are chosen such that the maximum field strength at the poles is 8.4 Gauss and 2.2 Gauss at the equator.

[15] Volumetric heating of the model corona is introduced in a way that attempts to mimic the effects of energy absorption above the transition region, thermal conduction, and radiative losses as well as satisfying known constraints of coronal heating. The heating function has the following form,

$$Q = \rho q_0 \left(T_0 - \gamma\frac{p}{\rho}\right) \exp\left[-\frac{(r - R_\odot)^2}{\sigma_0^2}\right], \quad (7)$$

where the target temperature, T_0, is 5.0×10^6 K poleward from a critical angle $\theta_0(r)$ which defines the coronal hole boundary, while $T_0 = 2.85 \times 10^6$ K equatorward of $\theta_0(r)$ in the streamer belt. The heating function is defined with $q_0 = 10^6$ ergs g^{-1} s^{-1} K^{-1}, where $R_\odot$ is equal to the solar radius and r is the heliocentric radius. The function $\theta_0(r)$ is defined as follows: for the region $R_\odot < r < 7R_\odot$,

$$\sin^2(\theta_o) = \sin^2(17.5^\circ) + \frac{(1 - \sin^2(17.5^\circ))(r - 1)}{8}, \quad (8)$$

which is equal to 17.5° at the solar surface and increases to a value of $\theta_o = 61.5^\circ$ at $r = 7R_\odot$. Beyond this radius, θ_o increases more slowly as

$$\sin^2(\theta_o) = \sin^2(61.5^\circ) + \frac{(1 - \sin^2(61.5^\circ))(r - 7)}{40}, \quad (9)$$

reaching a value of $\theta_o = 90^\circ$ at $r = 47R_\odot$, which is then held fixed at 90° for $r > 47R_\odot$. The heating scale height function is kept constant in the streamer belt with $\sigma_0(r, \theta) = 4.5$, and increases inside the coronal hole as

$$\sigma_0(r, \theta) = 4.5\left(2 - \frac{\sin^2(\theta)}{\sin^2(\theta_o)}\right), \quad (10)$$

which gives a scale height for the volumetric heating that varies from $4.5R_\odot$ near to equator to $9R_\odot$ at the poles. It is important to mention that this heating function was designed with several free parameters with the desire of reproducing observed features of the fast and slow solar wind.

3.1. Computational Mesh

[16] The computational domain for the simulation extends from $-32R_\odot < x < 32R_\odot$, $-32R_\odot < y < 32R_\odot$, and $-32R_\odot < z < 32R_\odot$ with the Sun placed at the origin with the magnetic axis aligned with the z axis. The system is initially resolved with 15,555 self-similar $4 \times 4 \times 4$ blocks containing a total of 995,520 cells. The blocks are distributed in size over seven levels of refinement with each subsequent level of refinement using cells half the size of the previous level (in each dimension). In this case, cells range in size from $1/32R_\odot$ to $2R_\odot$ and are spatially positioned to highly resolve the central body and the flux rope as well as the heliospheric current sheet. The grid is refined every 200 iterations without coarsening for the first 10,000 iterations to increase the total number of cells to 1.9 million. Beyond 10,000 iterations, the grid is refined and coarsened such that the total number of cells is held nearly constant. AMR criteria are chosen so that blocks close to the y axis with large time variations in density are preferentially refined. In this way, the high-resolution mesh tracks the shock directly in front of the flux rope as well as the central part of the flux rope.

3.2. Boundary Conditions

[17] To pose a physically meaningful system subject to the equations of ideal MHD, it is necessary to specify appropriate boundary conditions at the inner boundary (the spherical surface $r = R_\odot$) and the outer boundary (the outer surfaces of the rectangular domain). The coronal boundary conditions are a function of heliospheric latitude. In the coronal holes poleward of θ_0, the following values are prescribed just inside $r = R_\odot$: $\rho = 2.5 \times 10^{-16}$ gm cm^{-3}, $p = 5.89 \times 10^{-2}$ dynes cm^{-2}, $\boldsymbol{u} = 0$, and $\boldsymbol{B} = \boldsymbol{B}_0$. These values are then allowed to interact with the solution inside our

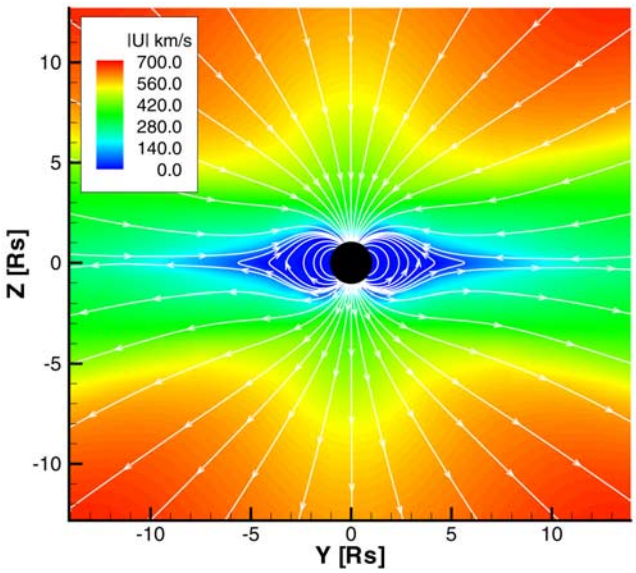

Figure 1. Magnetic structure and velocity for the steady-state solar wind solution. Solid white lines are magnetic "streamlines" drawn in the $y - z$ plane superimposed upon a false color image of the velocity magnitude. Note the bimodal nature of the solar wind.

physical domain through the $r = R_\odot$ boundary; this approach ensures that the appropriate information from the "solar" values is propagated into the solution domain by the numerical flux function used in the scheme. These conditions set up a pressure gradient that drives plasma away from the Sun and permits plasma to pass through the boundary as the mass source for the solar wind. The magnetic field at the surface is specified by the time-independent multipole expansion for the intrinsic field given by equation (6). In the streamer belt equatorward of θ_0, the following values are prescribed just inside $r = R_\odot$: $\partial\rho/\partial r = 0$, $\partial p/\partial r = 0$, $\boldsymbol{u} = -\boldsymbol{u}_{outside}$, $\boldsymbol{B} = \boldsymbol{B}_{outside}$, where the subscript *outside* refers to the values just outside $r = R_\odot$, which are computed by the flow solution scheme. These conditions strictly enforce a zero flow at the boundary, both in the radial and tangential directions; they also enforce continuity of the magnetic field across $r = R_\odot$. This provision allows the magnetic field of the flux rope (prescribed in the streamer belt) to pass through the interface where the footpoints are effectively "line tied." At the outer boundary of the domain, the flow is super-fast. Thus all waves are exiting the domain, and no information from outside the domain propagates into the domain.

3.3. Steady-State Solar Wind Solution

[18] The solar wind solution is produced by the time evolution of the system subject to the described heating function, intrinsic magnetic field, and boundary conditions. An initial plasma flow is taken to have mass density falling off as $1/r^3$, constant temperature, and a radial outflow with the velocity proportional to r. Local time stepping is used to speed up convergence, achieving a near steady-state solution after 84,000 iterations, with AMR periodically applied with an emphasis on resolving the heliospheric current sheet. Figure 1 depicts a two-dimensional (2-D) cut through the 3-D steady-state solar wind model in the meridional plane close to the Sun. The false color image indicates the velocity magnitude, $|\boldsymbol{u}|$, of the plasma while the magnetic field is represented by solid while lines. Inspection reveals a bimodal outflow pattern with slow wind leaving the Sun below 400 km/s near the equator and high-speed wind above 700 km/s found above 30° latitude. In this model, we find that the source of the slow solar wind is cooler plasma originating from the coronal hole boundaries that overexpands and fails to accelerate to high speed as it fills the volume of space radially above the streamer belt. This model has similarities to the empirical model of the solar wind proposed by *Wang and Sheeley* [1994] that explains solar wind speeds as being inversely related to the expansion of contained magnetic flux tubes. The magnetic field remains closed at low latitude close to the Sun forming a streamer belt. At high latitude, the magnetic field is carried out with the solar wind to achieve an open configuration. Closer to the equator, closed loops are drawn out and (at a distance of $r > 3R_\odot$), collapse into a field reversal layer. The resulting field configuration has a neutral line and a current sheet originating at the tip of the streamer belt similar to numerical solution originally obtained by *Pneuman and Kopp* [1971].

4. Flux Rope of Gibson and Low

[19] To initiate a CME within this coronal model, we superimpose a 3-D magnetic flux rope and its entrained plasma into the streamer belt of our steady-state coronal model (see Figure 2). The flux rope we employ comes from the GL family of analytical solutions of the ideal MHD equations describing an idealized, self-similar expansion of a magnetized cloud resembling a CME. We briefly describe here the mathematical form of the GL solutions while more complete derivations and descriptions of the solutions can be found in their original paper [*Gibson and Low*, 1998].

4.1. Self-Similar Flux Ropes

[20] The CME models of GL are developed by finding a 3-D analytical solution to the equation

$$\frac{1}{4\pi}(\nabla \times \boldsymbol{B}) \times \boldsymbol{B} - \nabla p - \rho \boldsymbol{g} = 0 \qquad (11)$$

and Maxwell's equation, $\nabla \cdot \boldsymbol{B} = 0$, that describe a global magnetostatic corona containing a magnetic flux rope in force balance with the pressure and weight of the plasma.

[21] The solution for this flux rope is derived by applying a mathematical stretching transformation $r \rightarrow r - a$ to an axisymmetric, spherical ball of twisted magnetic flux in equilibrium with plasma pressure. The transformation, performed in spherical coordinates (r, θ, ϕ), draws space toward the origin while holding angular coordinates θ and ϕ fixed. This mathematical procedure serves two important purposes. First, it generates a geometrically complex solution by distorting the originally spherical, axisymmetric flux rope (centered away from the heliocentric origin) into a tear-drop shape with full 3-D spatial variation. The magnetic structure, seen as a 3-D representation in Figure 2, possesses a toroidal core shown in solid blue lines surrounded by flux becoming progressively more twisted closer to the flux rope surface shown as solid red lines. The computational grid is seen in Figure 2 as black lines superimposed upon a false color image

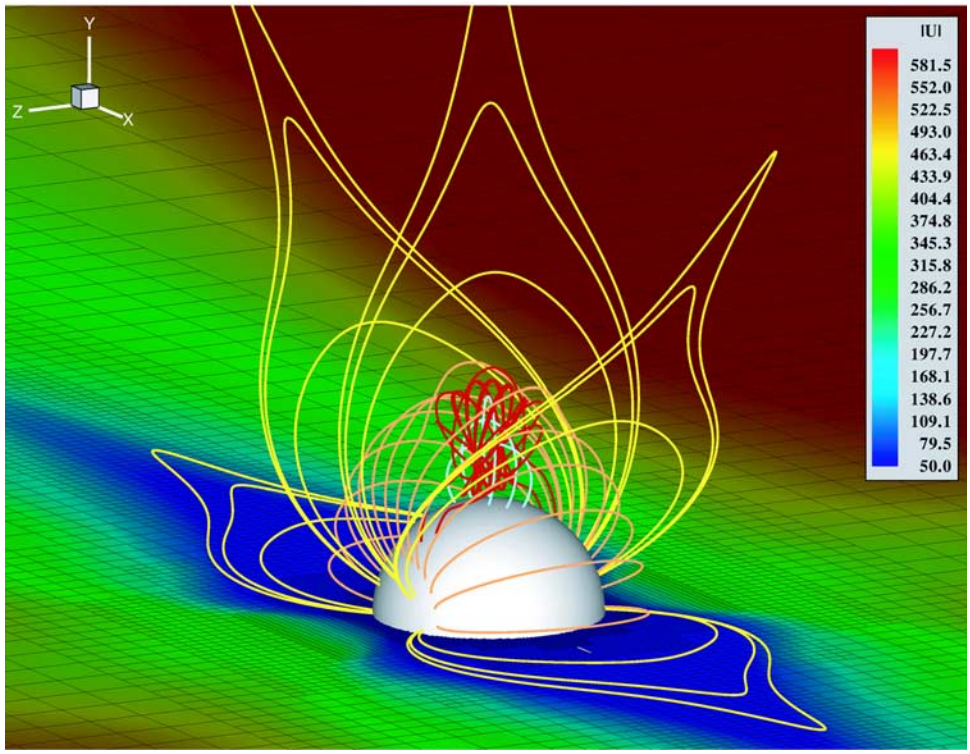

Figure 2. Depicted is a three-dimensional (3-D) representation of the coronal magnetic field drawn as solid colored lines at $t = 0$ hours. The flux rope is drawn with blue and red lines showing a sheared (toroidal) core surrounded by a highly twisted sheath, respectively. Orange and yellow lines show the poloidal field of the steady-state equatorial streamer belt. On the $x - z$ plane, the computational mesh is drawn with black lines superimposed upon a false color image the velocity magnitude.

of the velocity magnitude. The second benefit of the stretching transformation is the introduction of Lorentz forces associated with the magnetic field that requires both the pressure and weight of plasma in a $1/r^2$ gravitational field to be in static equilibrium. Where the magnetic field is concave away from the solar center, cold dense plasma is required to offset the upward directed magnetic tension. By contrast, where the field is convex away from the Sun, the plasma density is reduced so that buoyancy offsets the downward directed Lorentz force. The given vertical orientation of the flux rope (see Figure 2) requires a density-depleted cavity in the upper extremity of the rope, while a dense core exists in the lower portion as seen in Figure 3. Figures 3a and 3b show meridional and equatorial slices of the corona, respectively, in which the density is represented as a false color image superimposed with white lines representing the magnetic field. These ''streamlines'' are generated by integrating the field on the plane while ignoring the component perpendicular to the plane. The density structures are an attractive feature of the model in that it possesses a dense helmet streamer containing a cavity embedded with a prominence-type density enhancement. Such long-lived coronal structures are often observed to give rise to CMEs [cf. *Hundhausen*, 1993].

[22] Within the GL formulation, the CME is modeled by prescribing an initial velocity field that is purely radial and increases linearly and infinitely with distance from the solar center. With such a velocity profile and with $\gamma = 4/3$, the expansion of the system evolves in a self-similar manner in which the entire atmosphere with its magnetic structure is carried out to infinity. The value of the GL CME model is that it captures both the morphology and kinematic properties of a variety of CMEs. In particular, it reproduces the canonical three-part density structure (front-cavity-core) and captures the early coherent phase of CME evolution. Some limitations of the model are its inability to address CME initiation and interaction of CMEs with a background solar wind as well as not treating magnetic reconnection.

[23] With our inclusion of the GL flux rope to a numerical, steady-state model of the corona and solar wind, we can extend the GL model to address these issues. To begin, we do not prescribe a flow field to the flux rope and surrounding corona but rather the CME results from an initial force imbalance due to a removal of part of the plasma in the flux rope and also from insufficient background coronal plasma pressure to offset the magnetic pressure of the flux rope. Since the simulation begins with the system in a state of force imbalance, the model does not specifically address a mechanism for CME initiation. However, the model possesses 3-D magnetic field topology and quickly relaxes to capture the energetics of a CME shortly following initiation. Such initiation might be related to a loss of equilibrium resulting from the drainage of prominence mass that anchored the flux rope down as proposed by *Low* [2001] and numerically simulated in 2-D by *Fan and Low* [2003]. Another possibility is the formation of a flux rope in the corona by magnetic reconnection as addressed by *Lin and Forbes* [2000] and *Linker et al.* [2003].

[24] Our chosen initial state does offer some advantages over simpler potential and force-free magnetic configura-

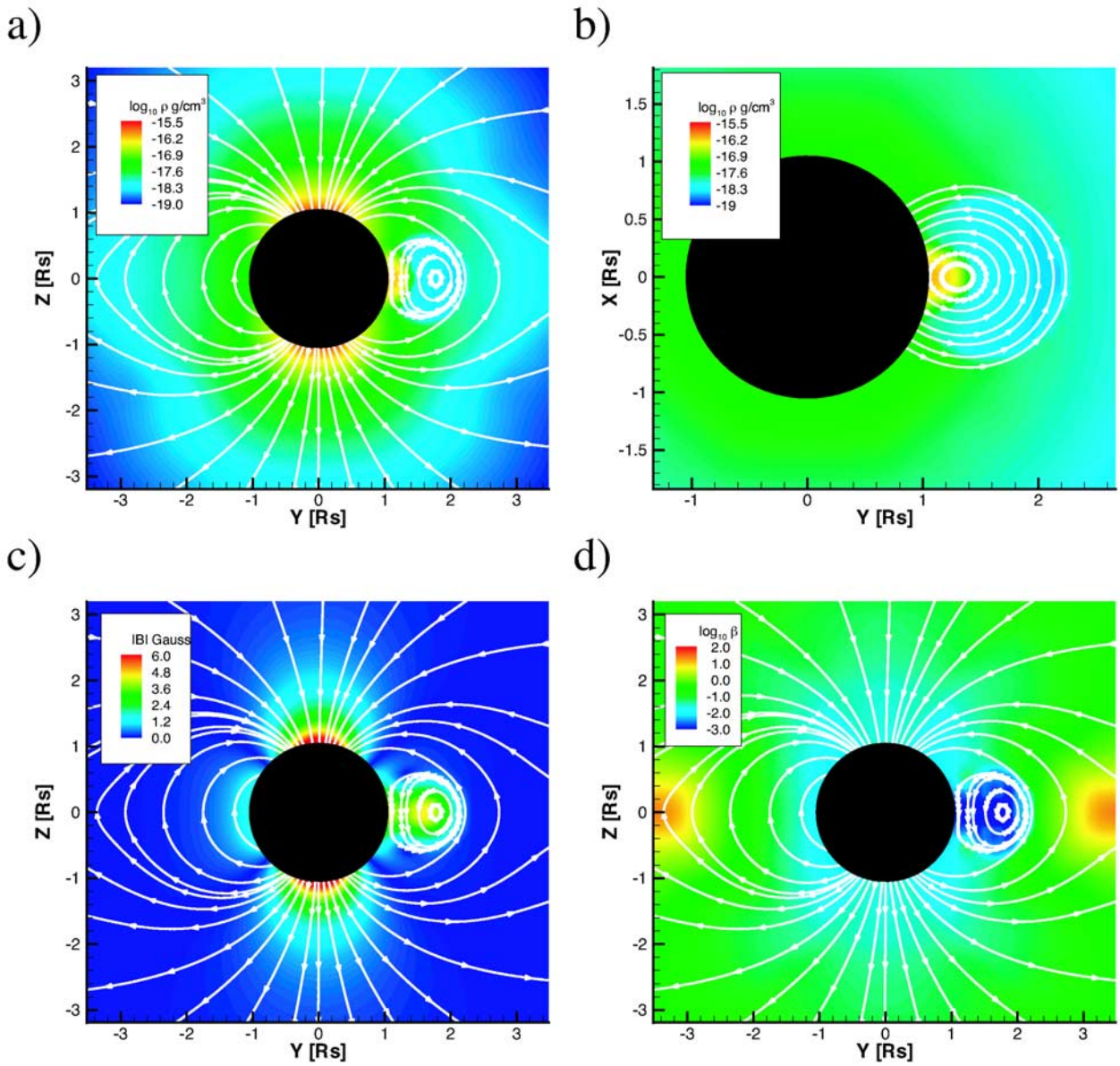

Figure 3. The initial coronal plasma density is depicted in Figures 3a and 3b with false color images in the $y - z$ meridional plane and the $x - y$ equatorial plane respectively. Figures 3c and 3d show the initial field strength and plasma β respectively in false color in the $y - z$ meridional plane. In all panels, the magnetic field is represented by "streamlines" drawn as solid white lines.

tions in that it possesses substantial free magnetic energy that is liberated as the flux rope expands. As the CME leaves the corona, it strongly interacts with the highly structured solar wind ahead of it, most notably, by the formation of an MHD shock running ahead of the flux rope. Our MHD simulation also allows us to mimic magnetic reconnection, in this case, through numerical resistivity. We will show in the next section, that reconnection plays a significant role in the restructuring of the coronal magnetic field following the CME.

4.2. Mathematical Form of the GL Flux Rope

[25] The flux rope is obtained by transforming a toroidal magnetic rope contained in a sphere of radius r_0. The center of the sphere is located at a radial distance of r_1 on the y axis. The plasma pressure in the flux rope is proportional to the free parameter a_1^2, which also controls the magnetic field strength in the flux rope through pressure balance.

[26] Mathematically, the flux rope magnetic field is written in terms of a scalar function A in spherical coordinates (r', θ', ϕ') as

$$\boldsymbol{b} = \frac{1}{r' \sin(\theta')} \left(\frac{1}{r'} \frac{\partial A}{\partial \theta'} \hat{r}' - \frac{\partial A}{\partial r'} \hat{\theta}' \alpha_0 A \hat{\phi}' \right), \tag{12}$$

where

$$A = \frac{4\pi a_1}{\alpha_0^2} \left(\frac{r_0^2}{g(\alpha_0 r_0)} g(\alpha_0 r') - r'^2 \right) \sin^2(\theta') \tag{13}$$

and

$$g(\alpha_0 r') = \frac{\sin(\alpha_0 r')}{\alpha_0 r'} - \cos(\alpha_0 r'). \quad (14)$$

The pressure inside the flux rope necessary for equilibrium is $\Pi = a_1 A$, where a_1 is a free parameter that determines the magnetic field strength and plasma pressure in the flux rope. Here, r_0 is the diameter of the spherical ball of flux and α_0 is related to r_0 by $\alpha_0 r_0 = 5.763459$ (this number is the smallest eigenvalue of the spherical Bessel function, $J_{5/2}$). The coordinate (r', θ', π') is centered relative to the heliospheric coordinate system on the y axis at $y = r_1$ and oriented such that the circular axis of the flux rope is in the heliospheric equatorial plane.

[27] In the next step, this axisymmetric flux rope is subjected to the mathematical transformation $r \rightarrow r - a$ that draws space toward the heliospheric origin and distorts the sphere containing the rope to a tear-drop shape. Following this transformation, the magnetic field takes the form:

$$B_r(r, \theta, \phi) = \left(\frac{\Lambda}{r}\right)^2 b_r(\Lambda, \theta, \phi), \quad (15)$$

$$B_\theta(r, \theta, \phi) = \left(\frac{\Lambda}{r}\frac{d\Lambda}{dr}\right) b_\theta(\Lambda, \theta, \phi), \quad (16)$$

$$B_\phi(r, \theta, \phi) = \left(\frac{\Lambda}{r}\frac{d\Lambda}{dr}\right) b_\phi(\Lambda, \theta, \phi), \quad (17)$$

where $\Lambda = r + a$ and (r, θ, ϕ) are the heliospheric spherical coordinates. Equilibrium within this transformed state demands that the plasma pressure be of the form

$$p = \left(\frac{\Lambda}{r}\right)^2 \left(1 - \left(\frac{\Lambda}{r}\right)^2\right)\left(\frac{b_r^2}{8\pi}\right) + \left(\frac{\Lambda}{r}\right)^2 \Pi \quad (18)$$

and that density be of the form

$$\rho = \frac{1}{F(r)}\left[-\left(\frac{\Lambda}{r}\right)^2\left(1 - \left(\frac{\Lambda}{r}\right)^2\right)\frac{d}{d\Lambda}\left(\Pi + \frac{b^2}{8\pi}\right) + 2\Pi\frac{\Lambda a}{r^3} + \frac{\Lambda a}{4\pi r^3}\left(1 - 2\left(\frac{\Lambda}{r}\right)^2\right)b_r^2 + \left(\frac{\Lambda}{r}\right)^2\left(\frac{a^2}{r_2} + \frac{2a}{r}\right) \cdot \left(\frac{b_\theta^2 + b_\phi^2}{4\pi\Lambda}\right)\right], \quad (19)$$

where $F(r) = GM/r^2$, with G being the gravitational constant and M being the solar mass. It is interesting to note that equation (19) does not depend on the density of the pretransformed state because without gravity, density is not specified, since there is no force associated with it. Only after gravity is introduced in the transformed state is density specified, and then it is done so to provide force balance in the radial direction.

[28] For this simulation, the flux rope is specified by setting $a = 0.3$, $r_0 = 1.0$, $r_1 = 1.6$ and $a_1 = 0.4$. The flux rope and contained plasma are superimposed upon the exiting corona, the results of which can be seen in Figures 2 and 3. The density of mass contained in the flux rope is further multiplied by a factor of 0.8, leaving the prominence buoyant. In addition, the equilibrium state of GL requires a significant outward increasing plasma pressure to offset the magnetic pressure in the upper portion of the magnetic flux rope. The background corona is insufficient to provide this pressure and results in a negative pressure when the GL solution is superimposed on the corona. To avoid negative pressure, we limit the depletion of pressure and density in the coronal cavity to 25 percent of the initial coronal values, which leaves the upper portion of the flux rope with unbalanced magnetic pressure.

[29] By introducing the GL solution to the corona, we have added 9.0×10^{31} ergs of magnetic and -4.8×10^{29} ergs of thermal energy, as well as 4.9×10^{14} gm of plasma to the corona. The added plasma is concentrated in a prominence-type core at the base of the flux rope that is approximately 10 times denser than the ambient corona. The magnetic field strength of the flux rope is quite conservative with a maximum value of only 5 Gauss, which is consistent with field measurements in quiescent prominences [*Leroy et al.*, 1983]. However, the magnetic field of the rope completely dominates the corona, being considerably stronger than the ambient coronal field and also dominating the plasma pressure as seen in Figures 3c and 3d. These figures show meridional slices of the corona with false color images of the field strength and plasma β, respectively, with solid white lines representing the magnetic field.

5. Simulation of the CME Event

[30] In this section, we present the results of a 3-D numerical simulation designed to study the evolution of a flux rope placed in the corona out of equilibrium. We find that the flux rope is expelled from the corona in a convincing fast CME-like eruption. The front of the rope rapidly achieves a maximum speed over 1000 km/s before decelerating and asymptotically approaching a terminal velocity near 600 km/s. A strong MHD shock front forms ahead of the flux rope as it travels through the solar wind. We will present an energy budget, which clearly shows the CME is magnetically driven with an interesting interaction with the plasma thermal energy. A current sheet forms at the base of the expanding flux rope where magnetic reconnection partially severs the rope from the line-tied coronal boundary. Finally, we present synthetic images of the Thomson-scattered white light showing how the CME would appear in a coronagraph.

5.1. CME Morphology

[31] Figure 4 presents a 3-D view of the CME as seen at $t = 2.0$ hours, from a perspective looking down and ahead from above the y axis, along which the CME is traveling. The false color image shows the velocity magnitude along with the numerical grid (shown in grey lines) on the equatorial ($x - y$) plane. A shock front is clearly visible preceding the flux rope in the color image as is the adaptive mesh tracking the shock. The magnetic field in the interior of the flux rope is represented by solid colored magenta

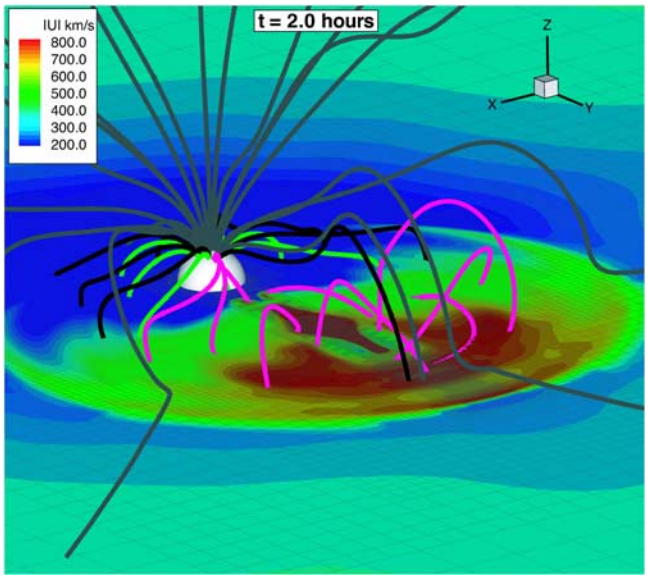

Figure 4. 3-D representation of the magnetic field lines 2 hours after the initiation of the CME. The color code represents the velocity magnitude in the $x - y$ plane and grey lines depict the computational mesh. Magenta lines show magnetic field lines of the flux rope while black and green lines show magnetic lines of the helmet streamer. Grey lines represent the open magnetic flux extending from the pole.

lines. The field close the the axis of the flux rope clearly has a strong toroidal component while the field at the surface is nearly poloidal. Grey lines show the open field lines of the solar wind some of which pass through the shock front where the lines bend sharply to wrap around the expanding flux rope. Black and green lines show closed field lines of the streamer belt.

[32] The time evolution of the CME is displayed in Figures 5 and 6 with a time series of figures showing the system at t = 1.0, 2.0, 3.0, and 4.0 hours. Figure 5 depicts the system in 2D meridional slices ($y - z$ plane), while Figure 6 shows equatorial slices ($x - y$ plane). In both cases, false color images show the plasma velocity magnitude upon which solid while lines are superimposed representing the magnetic field.

[33] We find the flux rope rapidly expanding and being expelled from the corona while decelerating. An MHD shock front moves ahead of the flux rope, traveling at nearly the same speed as the rope on the y axis while propagating far ahead to the sides of the rope. In effect, the shock front moves at relatively uniform speed, initially forming a spherical bubble, while the flux rope inside the front moves forward faster than it expands to the sides. We also find that the structure of the ambient solar wind has a profound influence on the shock front. The wind and magnetosonic speeds are minimal in the heliospheric current sheet, and both grow with heliospheric latitude. As a result, the shock travels at higher latitude in the fast solar wind with a lower Mach number than found at low latitude. For example, at t = 1.0 hour, the shock travels at approximately 1100 km/s through the current sheet with a magnetosonic Mach number of 6.04 while at this same time, the magnetosonic Mach number at 30° latitude is only 1.86.

[34] The variation in Mach number is clearly reflected in the temperature structure of shock heated plasma shown in Figure 7. This figure depicts a 2-D meridional slice at t = 1.0 hour where solid white lines representing the magnetic field are superimposed upon a false color image of the temperature. Inspection of Figure 7 reveals that the temperature of the shock-heated plasma is greatest at the heliospheric current sheet where the Mach number is the largest and the temperature reaches 2.1×10^7 K. The temperature behind the shock then rapidly decreases with latitude, reaching a value of 1.3×10^7 K at 30° heliolatitude. The temperature behind the shock rapidly falls with radial distance, as the CME moves from the Sun as is seen in Figure 8. This line plot shows the temperature as a function of height behind the shock front where it travels along the current sheet.

[35] There is a clear dimple (concave-outward) in the shock front very near the heliospheric current sheet seen in the meridional slices for $t > 1.0$ hour. At this location the plasma β is high and the shock speed is super-fast and is above the critical speed defined by

$$v_{crit}^2 = \left(\frac{\gamma+1}{\gamma-1}\right)c_a^2 - \left(\frac{2}{\gamma-1}\right)c_s^2, \tag{20}$$

where c_a and c_s are the Alfvén speed and sound speed, respectively, defined as $c_a = \sqrt{B^2/4\pi\rho}$ and $c_s = \sqrt{\gamma k_B T/m_i}$. Here, k_B is Boltzmann's constant and m_i is the ion mass. The shock speed is outside the switch-on regime, indicating a fast mode along the leading shock front except at the current sheet where the shock is hydrodynamic in nature. Close inspection of Figure 5 reveals that at high latitude, the magnetic field lines bend at the shock to deflect around the flux rope. At low latitude, where the shock front forms a dimple, the field lines deflect toward the equatorial plane and only bend to go around the flux rope well behind the shock. Previous studies have found that in the switch-on regime, the shock is of the intermediate type in the concave region, becoming a fast shock in the convex portion of the front [*Steinolfson and Hundhausen*, 1990; *DeSterck et al.*, 1998; *Fan and Low*, 2003]. However, in our case, the shock dimple is largely the result of spatial variations in the background solar wind near the heliospheric current sheet. Close to the Sun, the shock travels faster away from current sheet where the magnetosonic speed increases relative to the current sheet itself where $\boldsymbol{B} = 0$. On a larger scale, the shock travels faster at higher latitudes in the higher temperature and higher speed wind than compared with the low-latitude wind. This effect leads to the dimple becoming a very broad indentation in the shock front by t = 4.0 hours. This same large-scale concave feature of the shock front has been found in earlier work such as *Odstrcil et al.* [1996] and *Riley et al.* [2002].

[36] We also find that magnetic reconnection plays a significant role in the evolution of the CME. At t = 1.0 hour, the magnetic topology of the system is nearly identical to that of the initial state. As time progresses, we find that a current sheet forms between field lines attaching the flux rope to the coronal boundary. Examination of Figures 5 and 6 reveals that reconnection at this current sheet partially severs the flux rope from the boundary and reforms the

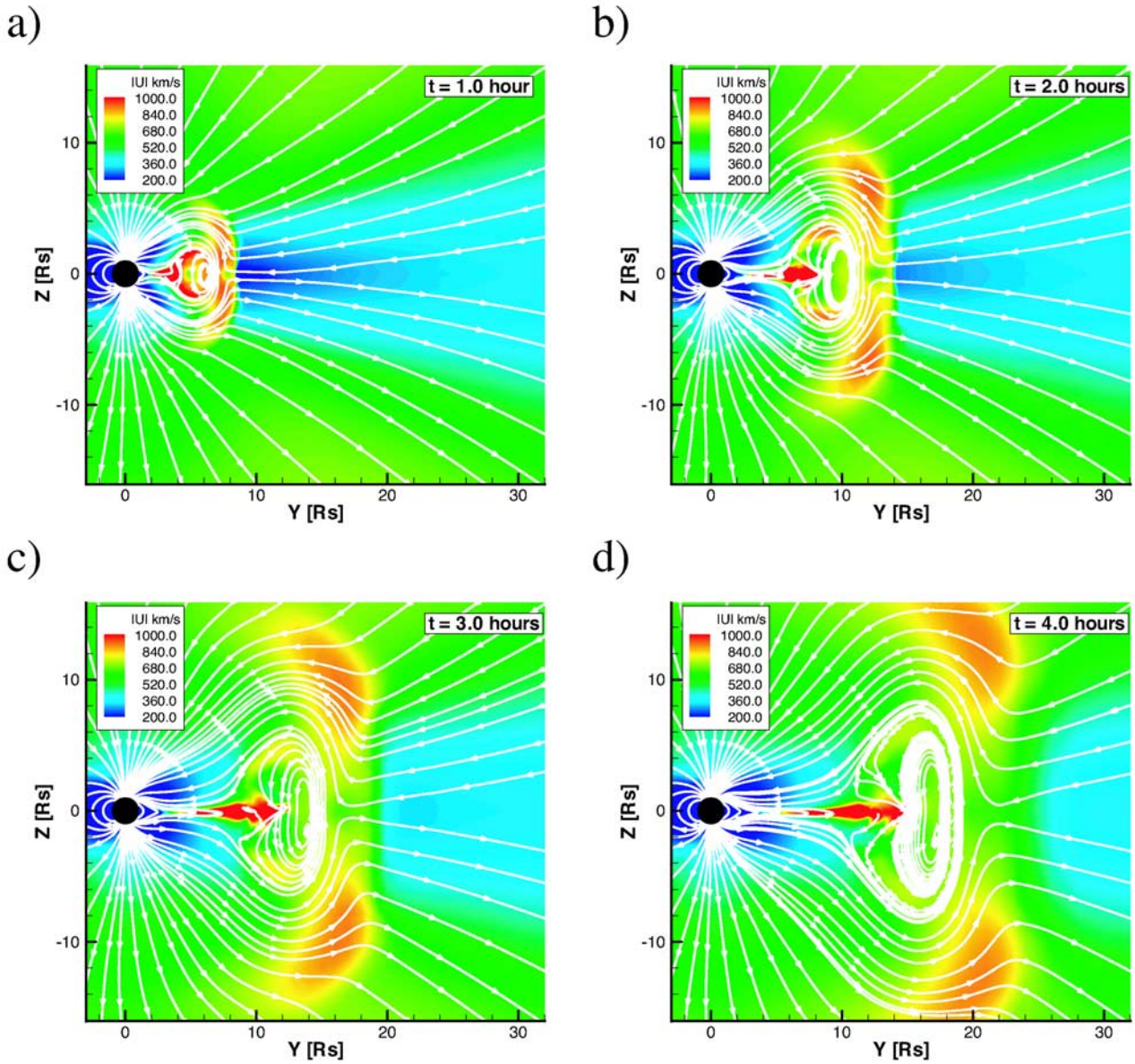

Figure 5. Time evolution of the CME in the $y - z$ meridional plane at (a) $t = 1$ hour, (b) $t = 2$ hours, (c) $t = 3$ hours, and (d) $t = 4$ hours. Solid white lines display magnetic "streamlines" superimposed upon a color image of the velocity magnitude on the $y - z$ plane.

helmet streamer. The cusp of the newly formed streamer is heated to more than 10^7 K (see Figure 7) by conversion of magnetic to thermal energy during the magnetic flux cancellation. This process nicely mimics the observed formation of potential-like x-ray arcades seen shortly after CMEs [*Sterling and Hudson*, 1997; *Moore et al.*, 2001]. We also find that a reconnection jet forms, which dimples in the back of the flux rope for $t > 1.0$ hour. It should be mentioned that the reconnection in these simulations occurs by way of numerical resistivity, which has been reduced by refining the grid with the use of time dependent AMR.

5.2. CME Acceleration

[37] Figure 9 shows the time evolution of the flow velocity at the front and center of the flux rope plotted as solid and dashed lines respectively. Here, we find that the flux rope front experiences a large initial acceleration taking its velocity to over 1200 km/s in just minutes followed by a more gradual deceleration. The velocity at the front then falls much more slowly from 1050 km/s to 800 km/s over the next 2 hours. The velocity curves show nearly equal levels of deceleration at the center and the front of the flux rope until $t = 2.0$ hours, when the center begins to move slightly faster than the front. Beyond this time, the flux rope begins to flatten as it is compressed in the front by a pile up of plasma. The spatial variation of the acceleration largely depends on the nature of the imposed initial force imbalance within the flux rope. The front of the flux rope expands very rapidly from unbalanced magnetic pressure, while the

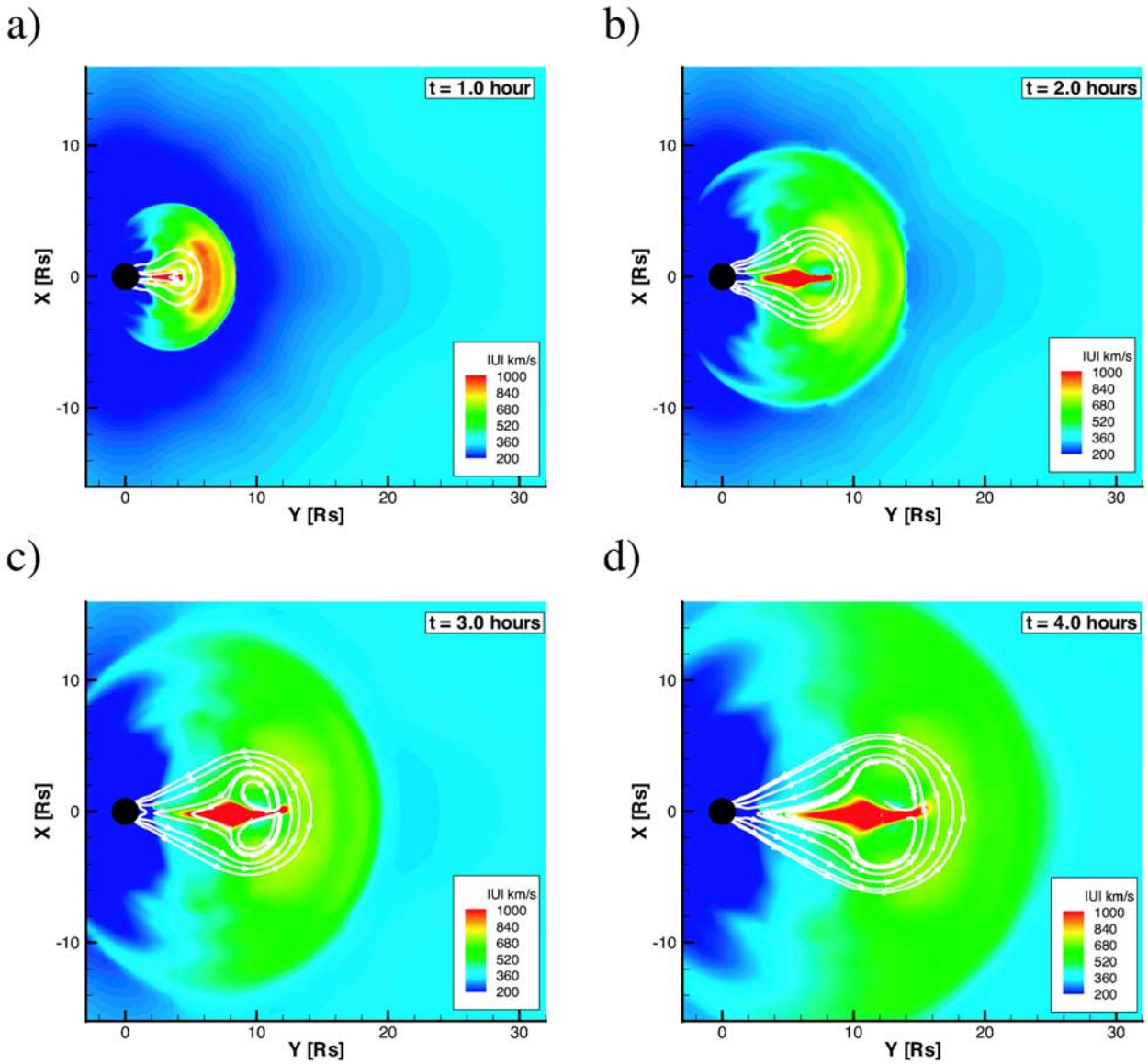

Figure 6. Depicted is a time sequence of panels showing the time evolution of the CME in the $x - y$ equatorial plane at (a) $t = 1$ hour, (b) $t = 2$ hours, (c) $t = 3$ hours, and (d) $t = 4$ hours. Solid white lines display magnetic "streamlines" superimposed upon a color image of the velocity magnitude on the $y - z$ plane.

back of the rope slowly accelerates as magnetic tension lifts the buoyant filament containing 4.9×10^{14} g of plasma. We also find the back of the flux rope briefly surpasses the front in speed as a result of reconnection between magnetic lines tying the rope to the solar surface. The reconnection drives a high-speed plume that collides with the back of the flux rope, propelling it forward and forming a concave-inward dimple. [*Riley et al.*, 2002] found similar reconnection-driven plumes in their CME model that extended all the way to 1 AU.

[38] To further illustrate the plasma flow associated with the model CME, we plot height/time curves for the front and center of the flux rope as well as the shock front directly ahead of the CME on the y axis (Figure 10). These plots again illustrate the initial precipitous fall from 1000+ km/s experienced by the flux rope followed by a more gentle deceleration. Before 2.0 hours, the front and center of the flux rope separate at a nearly constant rate, corresponding with a nearly uniform expansion of the rope. The shock front moves steadily ahead of the rope to a distance of $1.6R_\odot$ at $t = 1.0$ hour (for which period the front of the flux rope is located at $r < 7R_\odot$) and then moves to a distance of $4.8R_\odot$ ahead of the rope by 3.0 hours.

[39] The deceleration of our model CME can readily be compared with observations, and for this purpose we plot the velocity of the front of the flux rope as a function of height as a solid line in Figure 11. We also plot an empirical relationship found by *Sheeley et al.* [1999] that largely describes the deceleration of fast halo CMEs observed with

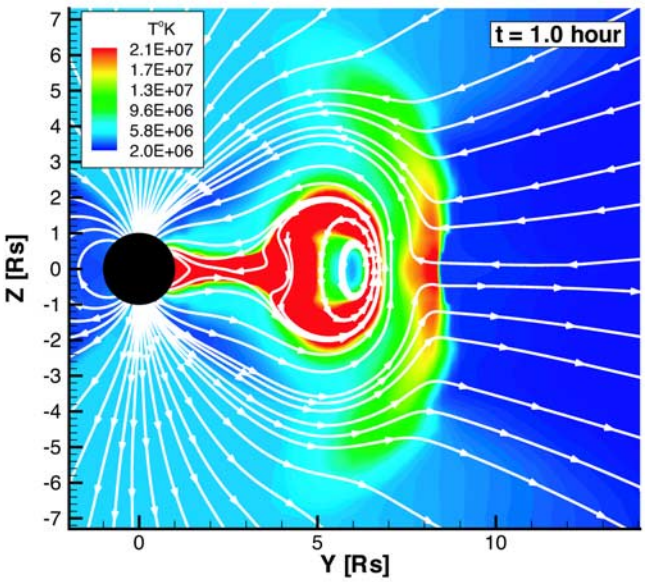

Figure 7. The plasma temperature is displayed in false color at $t = 1$ hour on the $y - z$ meridional plane. Solid white lines show magnetic "streamlines" on the same plane. Note the appearance of hot plasma at the center of the shock front and at the point magnetic reconnection where the helmet streamer reforms.

the Large-Angle Spectrometric Coronagraph (LASCO). The empirical relationship is given by the equations:

$$r(t) - r_0 + v_1 t + \left(1 - e^{-t/\tau}\right)(v_0 - v_1)\tau \tag{21}$$

$$v(t) = v_1 + (v_0 - v_1)e^{-t/\tau}. \tag{22}$$

For our model, we find $r_0 = 3.0R_\odot$, $v_0 = 1033.0$ km/s, and $v_1 = 583.0$ km/s and $\tau = 2.25$ hours gives a close fit to our numerical simulation for velocities less than 1030 km/s. In

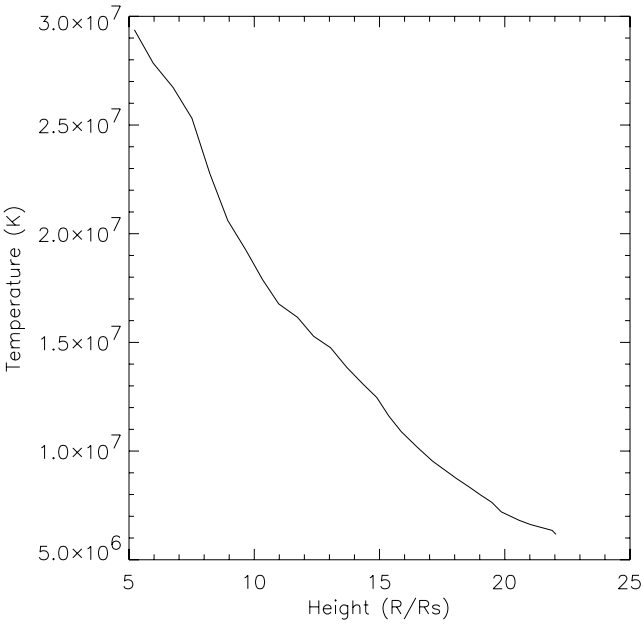

Figure 8. The temperature at the center of the shock front (on the y axis) is plotted as a function of height.

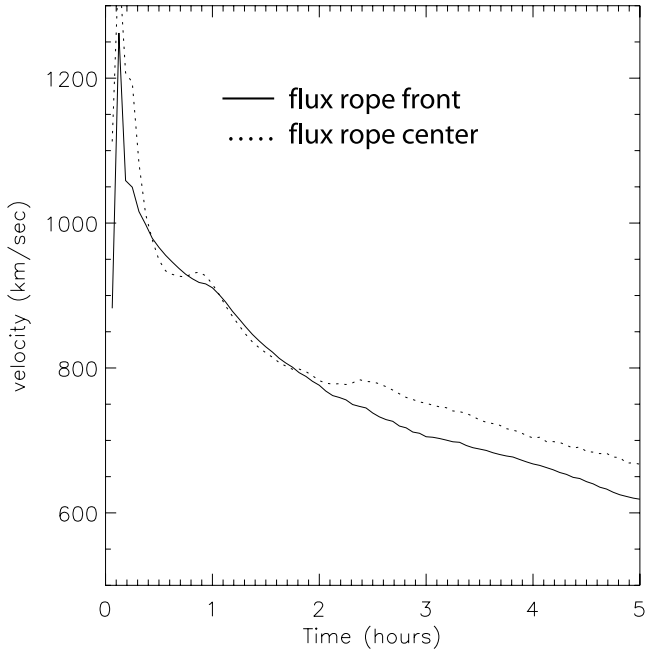

Figure 9. The radial velocity, u_r, along the y axis, is plotted as a function of time for both the front and center of the flux rope in solid and dashed lines, respectively.

comparison, *Sheeley et al.* [1999] give examples of the deceleration of fast CMEs that can be described with the following parameters: $r_0 = 2.6R_\odot$, $v_0 = 1098$ km/s, $v_1 = 598$ km/s and $\tau = 2.1$ hours, $r_0 = 5.6R_\odot$, $v_0 = 945$ km/s, and $v_1 = 595$ km/s and $\tau = 2.1$ hours. Clearly, our simulation produces a height/time curve that is very similar to the observed deceleration of these fast CMEs. The exception is

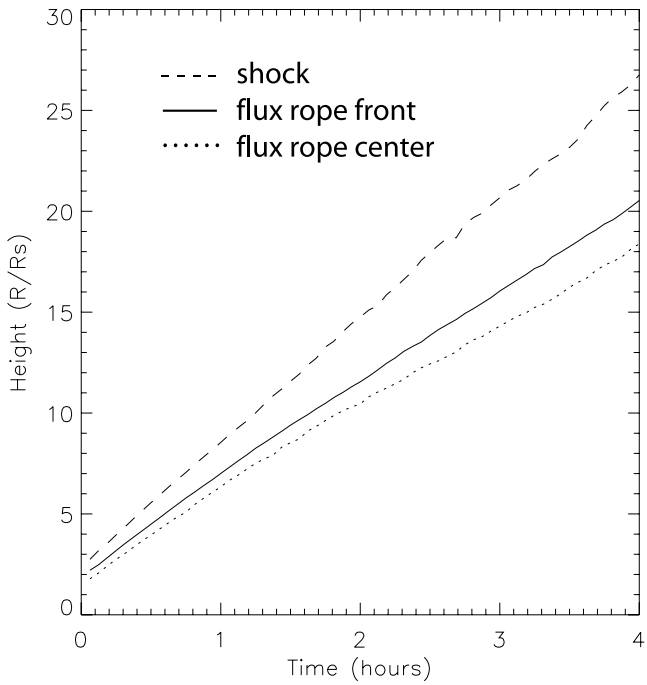

Figure 10. The height, r, along the y axis, is plotted as a function of time for the shock front along with the front and center of the flux rope.

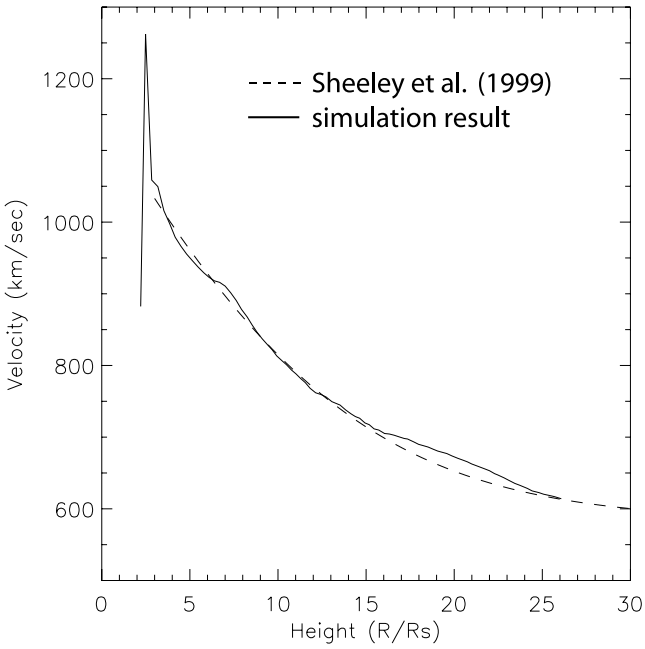

Figure 11. The radial velocity, u_r, at the front of the flux rope along the y axis is plotted as a function of height in a solid line. The dashed line shows an empirical relationship expressed by an exponential decay in velocity that closely approximates the evolution of the model CME [*Sheeley et al.*, 1999].

the extreme acceleration/deceleration that we find in the first 10 min of our simulation, which is beyond the range that is observed. This fact is not unexpected given that our model does not provide a smooth transition from equilibrium to eruption. However, the excessive acceleration is spatially limited to the front of the rope and is very short lived, after which the system relaxes to give a good representation of a fast CME.

[40] The deceleration of the flux rope front is well approximated (for $r > 3R_\odot$) by the empirical relation $a_{CME} = 55.6e^{-t/\tau}$ m s^{-2}, which can be compared to the Sun's gravitational acceleration, $a_{sun} = 274(R_\odot/r)^2$ m s^{-2}. In this case, the CME deceleration at $r = 3R_\odot$ is 200 m s^{-2} compared with solar gravity of 30 m s^{-2}. The exponential drop-off in CME deceleration would not fall below the solar deceleration until $r = 50R_\odot$, which is outside the computational domain. Thus the deceleration for the entire event is too large to be accounted for by ballistic motion in the Sun's gravitational field but rather is due to the mass of plasma swept up and shock heated ahead of the flux rope ("snowplow" effect). This finding corroborates the suggestion by *Sheeley et al.* [1999] that shock accumulated mass could explain the CME deceleration that they observed. The following analysis of the energetics of the system will shed further light on the driving and damping mechanisms governing the evolution of the CME.

5.3. Energetics of the CME

[41] Since the CME is undriven, the energy for the eruption must come from the preevent coronal initial state. Given this fact, examining the MHD energy components as a function of time is particularly instructive to determine the exchange of energy during the eruption. During the first hour there is a net change of $+4.0 \times 10^{31}$ ergs of kinetic energy, $+3.4 \times 10^{31}$ ergs thermal energy, and $+6.0 \times 10^{30}$ ergs of gravitational energy. The total kinetic+thermal+gravitational energy increase is is 8.0×10^{31} ergs, which is supplied directly from the magnetic energy of the flux rope, which is liberated as the flux rope expands. The CME is clearly driven by magnetic pressure pushing the flux rope out of the the corona, lifting its embedded mass while sweeping up additional shock heated plasma. The monotonic decrease in magnetic energy implies that the flux rope drives the CME for the duration of the simulation.

[42] The thermal energy exhibits a short lived increase of 4.0×10^{31} ergs followed by a gradual decrease in which the energy falls 2.5×10^{31} ergs above the initial value. The rise in thermal energy corresponds with the rapid acceleration of the flux rope front to over 1000 km s^{-1}, which is well above the magnetosonic speed of the corona. The resulting shock heats the plasma and largely gives rise to the increase in thermal energy. As the CME decelerates, the Mach number characterizing the shock falls as does the shock heating rate. This heating reduction, combined with adiabatic cooling behind the shock, allows the thermal energy to approach the steady-state value.

[43] The kinetic energy of the CME, is a factor of 6 times larger than the work required to lift its mass in the Sun's gravitational field. This fact is consistent with the high speed of the CME, which is well above the surface escape velocity of the Sun $\sim$600 km s^{-1}. Thus gravity is overwhelmed and the pile up of shock heated plasma dominates the deceleration of the CME. The pile up of plasma is clearly evident in the kinetic energy, which continues to increase for the entire duration of the simulation even as the CME decelerates. The kinetic energy reaches 5.0×10^{31} ergs at $t = 2.0$ hours when the velocity associated with the CME spatially varies from 750 to 920 km s^{-1}. Using a mean value for the velocity indicates that approximately 1.4×10^{16} g of plasma is ultimately accelarated by the CME. The mass gain is significant given that the flux rope initially contained $\sim 1 \times 10^{15}$ g. The mass increase comes from the surrounding helmet streamer and, more significantly, is swept up in the spatially extensive shock front that precedes the flux rope. For comparison, the entire mass of the steady-state system filling the entire computational domain is 3.4×10^{17} g. At present, no analysis has been published to determine whether fast CMEs increase in mass but research in that direction is currently being undertaken (X. Burkepile, private communication, 2003).

[44] A recent study of the energetics of CMEs observed by LASCO [*Vourlidas et al.*, 2000] found that for every event, gravitational potential and kinetic energies increased at the expense magnetic energy, which is consistent with our simulation. However, significant mass increase was found in only three of the eleven CMEs studied and no relationship between CME speed and mass increase was clear. In the case of *Vourlidas et al.* [2000], mass was only calculated in the region of space thought to be occupied by a flux rope, so it is not clear whether mass swept up outside of the rope could have been missed. In comparison with another global 3-D CME model, *Odstrcil and Pizzo* [1999] introduced a disturbance at their inner boundary placed near $30R_\odot$. In this case, swept up mass was not explicitly calculated but

their CME rapidly decelerated as it passed through a dense heliospheric plasma sheet while driving a shock. This behavior is qualitatively similar to the deceleration and shock formation that we find.

5.4. Synthetic Coronagraph Images of the CME

[45] We have produced a CME model with speeds that are characteristic of fast CMEs and we have found that in this case, strong shocks are driven in the low corona. It is rare that features of CMEs observed in the corona in Thomson-scattered white light are interpreted as signatures of shocks. As an example, *Sime and Hundhausen* [1987] observed a bright loop at the front of a CME that they identified as a candidate for a coronal shock. In this case, the presence of a shock was inferred from the high speed of the loop (1070 km/s) and the absence of any deflections preceding the CME; also the expanding loop did not cease its lateral motion to form stationary legs. More recent observations by multiple instruments on SOHO along with radio observations have made clear cases for shocks that appear as visible components of CMEs in LASCO images. In two reports, *Raymond et al.* [2000] and *Mancuso et al.* [2002], shocks were observed simultaneously in the low corona ($r < 3R_\odot$) by LASCO, the Ultraviolet Coronagraph Spectrometer (UVCS) and as type II radio burst. UVCS gave clear spectroscopic evidence for the presence of shock fronts associated with CMEs while radio bursts indicated the presence of shock-accelerated electrons. The shock fronts observed with LASCO by *Raymond et al.* [2000] and *Mancuso et al.* [2002] were representative of fast CMEs with speeds of 1200 km/s and 1100 km/s, respectively, which is comparable to the speed observed by *Sime and Hundhausen* [1987].

[46] A discussion of our work would be incomplete without mentioning the evolution of the plasma density associated with the shock front. Rather than simply displaying 2-D representations of the density in various planes, it is far more instructive to present the density as it would appear in a coronagraph image. To that end, we produce synthetic Thomson-scattered white-light images from three perspectives at three different times, which are displayed in Figure 12. Here, Figures 12a, 12b, and 12c show the corona viewed from the x axis at time t = 1.0, 2.0, 3.0 hours, respectively (''side view''). The same time sequence is presented in Figures 12d, 12e, and 12f, as viewed from the polar axis (''top view''), while a halo CME representation is given in Figures 12g, 12h, and 12i, viewed slightly off center from the y axis (''front view''). Each figure shows a gray scale image of the total scattered intensity of radiation, $I = I_t + I_r$, where I_t and I_r are radiation intensities polarized tangential to the solar limb and radial to the Sun, respectively. The intensities are found by the line-of-sight integration of the density multiplied by a scattering function that takes into account the extended light source of the limb-darkened solar disk as summarized by *Billings* [1966]. For these images, we have divided the background steady-state intensity to form a relative brightness.

[47] In the side view images, we find that the dense core of plasma (see Figures 3a and 3b) is not present in the line-of-sight images. The modest mass enhancement at the base of the flux rope has expanded to such an amount by 1.0 hour that its density is very near the background value. We find that a dense shell of plasma exists between the shock front and the flux rope followed by a density depleted cavity. The shock front has the same basic features, as first described by *Sime and Hundhausen* [1987], namely a bright loop expanding in the corona at super-Alfvenic velocity (>1000)km/s that expands laterally without forming stationary legs. A more rarefied region forms between the coronal boundary and the rear of the flux rope reflecting the large degree to which plasma is removed from the corona by the CME. There is also a narrow dark lane in the center of the ejecta that is seen in Figure 12a at t = 1.0 hour. This is a consequence of the CME passing through the plasma sheet and is qualitatively very similar to density images in the work of *Wu et al.* [1999].

[48] The polar view of the CME shows a surprisingly different morphology than is viewed from the side. Here, the enhanced density associated with the shock front stands out much more prominently and is seen to partially encircle the Sun. For the synthetic images, the line-of-sight integral is dominated by density over the limb of the Sun, near the plane of the sky. Consequently, the polar view preferentially shows the density structure in the heliospheric current sheet. As we mentioned before, the low magnetosonic speeds near the current sheet lead to considerably higher Mach numbers than are found at higher heliospheric latitude. Associated with the higher Mach number is a higher density compression [*Kabin*, 2001], which results in the brighter shock front in the polar view. The final column of Figures 12g, 12h, and 12i shows a dramatic view of the CME directed toward the observer as a halo event. In this case, we find that the intensity reflects a density structure strongly effected by the MHD shock interaction with the bimodal solar wind. Here, the front has an oval shape aligned with the polar axis, which is indented and brightened at the sides near where the front crosses the x axis. This morphology results from the enhanced density behind the shock front, which propagates with enhanced speed and lower Mach number in the high-latitude fast wind relative to the lower speed and higher Mach number of the shock (and greater density compression) in the low-latitude slow wind.

6. Discussion and Conclusions

[49] We have investigated the time evolution of a 3-D MHD model of a CME driven by the magnetic pressure and buoyancy of a flux rope in an initial state of force imbalance. The ensuing eruption originates in the low corona and develops as the flux rope and plasma are expelled through the solar wind. The model eruption possesses many features associated with fast CMEs. First, the preevent structure of our model, a dense helmet streamer possessing a cavity and dense core threaded by a six Gauss magnetic flux rope. In comparison, observations show that the majority of CMEs originate from helmet streamers that overlie quiescent prominences [cf. *Hundhausen*, 1993] thought to be supported by flux ropes [*Low*, 2001]. Second, the energy for the eruption comes from the preevent magnetic configuration and yields $\sim 5 \times 10^{31}$ ergs of kinetic and gravitational energy to drive $\sim 10^{16}$ g of plasma from the corona. Both the energy and mass that characterize the eruption are within the limits commonly observed for CMEs. The CME propagates to $32R_\odot$ through a realistic steady-state model of the

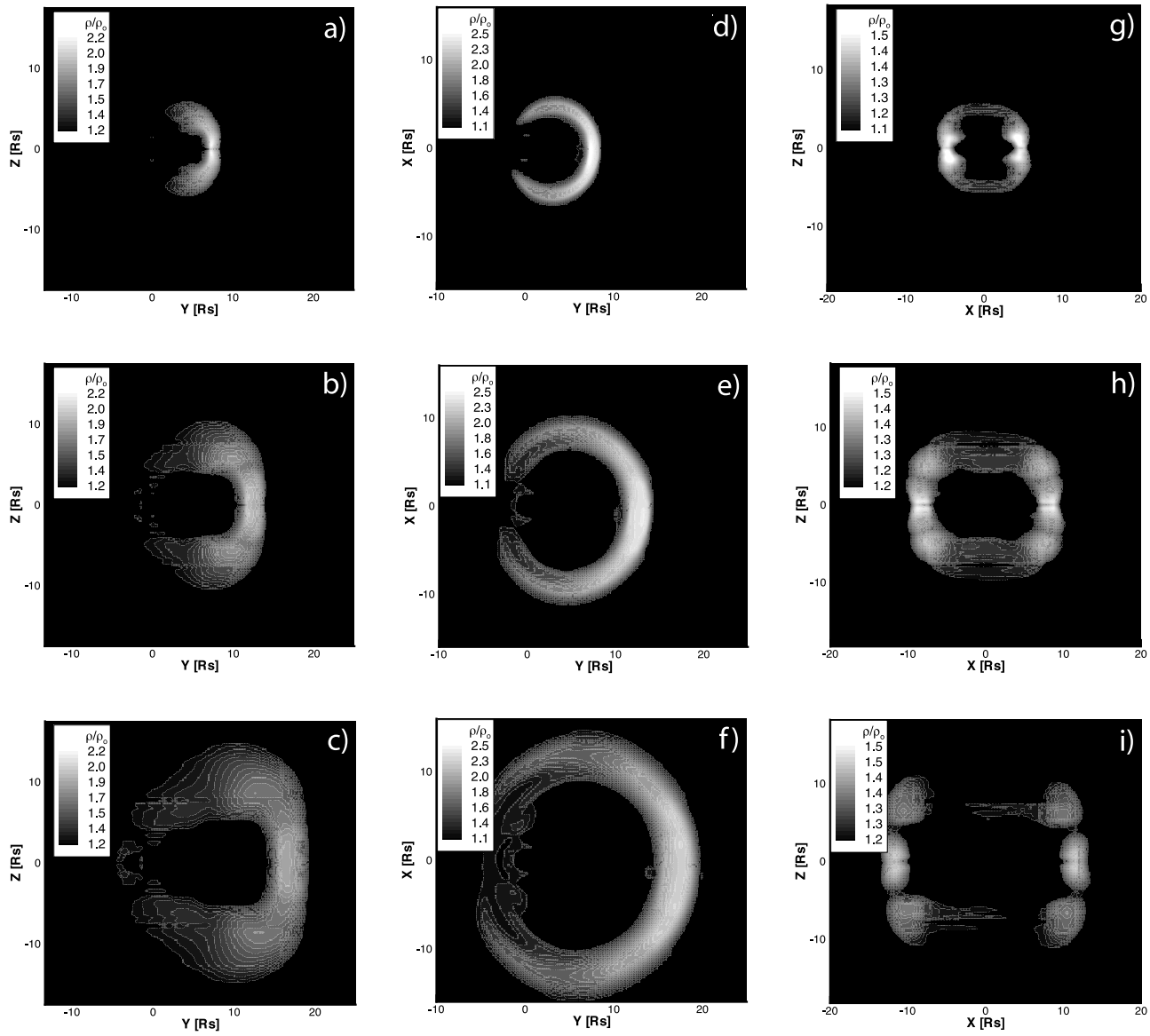

Figure 12. Synthetic images of the relative Thomson-scattered, white-light intensity as view from three different perspectives. Figures 12a, 12b, and 12c show the system viewed from the *x* axis, Figures 12d, 12e, and 12f are viewed from the *z* axis, and Figures 12g, 12h, and 12i are viewed slightly displaced from the *y* axis. Each perspective is shown at times $t = 1$, $t = 2$, and $t = 3$ hours in the top, middle, and bottom in the column of panels. Significant features are a pile up of plasma at the shock front ahead of the erupting flux rope A depletion of density is behind the expanding magnetic field.

corona with speed and deceleration that can be convincingly compared with a fast CME. We are then able to determine that plasma swept up in the shock front preceding the CME is essential for its deceleration. Furthermore, we find that the shock interacts with the bimodal solar wind in an interesting way that strongly influences the appearance of the CME in synthetic coronagraph images. Also, the model suggests that shocks associated with fast CMEs may heat the plasma to tens of millions of degrees K, which may have an observable signature in the X-ray spectrum. Finally, we note that the synthetic Thomson-scattered images show density structures that qualitatively represent a loop-cavity structure commonly observed for CMEs.

[50] Our 3-D MHD numerical model possesses many of the observed characteristics of high-speed CMEs, such as total mass and energy and is also representative of basic features as shock formation and related CME deceleration. The success of our model in capturing many properties of CMEs, including properties of preevent structures and background solar wind, suggests the model's possible value as a tool for studying CME propagation and space weather phenomena. We should also note that that initiating CMEs with the GL flux rope in our model corona has limitations. While suitable for modeling the declining phase of impulsive events, we have not reproduced realistic levels of initial CME acceleration. We find excessive acceleration results from the fact that the GL solution essentially describes a high-β equilibrium state, and placing it in a realistic coronal environment necessarily places it in a low-β regime. The subsequent state of force imbalance produces an accelera-

tion that is too large but ultimately yields an appropriate amount of energy. For the background pressure of our model corona and our choice of GL parameters, we find the flux rope can only be near equilibrium if the rope's field strength is near one Gauss. At two Gauss, the GL flux rope produces a low speed event in which magnetic reconnection provided a secondary, long-lasting acceleration for the CME.

[51] In the future, our research will explore the MHD processes by which CMEs make their way from the low-β corona to the high-β solar wind with emphasis on shock structure. Advanced AMR techniques will be applied to highly resolve shocks and allow us to capture highly structured, multiple shock fronts [*DeSterck et al.*, 1998] that may form. Larger-scale simulations will investigate the long-term fate of CMEs in interplanetary space. Fundamental questions need to be addressed concerning the interaction of the flux rope with the solar wind, including current sheet formation/dissipation, plasma swept up by the CME, and evolution of the 3-D density structure. Finally, we will investigate the space weather phenomena associated with CMEs by coupling our model to a magnetospheric model of the Earth. For such studies, we will introduce a much more realistic coronal magnetic field configuration based on synoptic magnetograms. Improvements to the solar wind model will follow, as we include nonthermal momentum terms associated with an Alfvén wave driven wind. These are some of the possibilities we will treat in our future investigations.

[52] **Acknowledgments.** We thank B. C. Low, Sarah Gibson, Thomas Zurbuchen, Tom Holzer, and Yuhong Fan for discussion and comments concerning the this research. The simulations reported here were carried out on an Origin2000 supercomputer at White Sands Missile Range Distributed Center. The research for this manuscript was supported by DoD MURI grant F49620-01-1-0359, NSF KDI grant NSF ATM-9980078, NSF CISE grant ACI-9876943, and NASA AISRP grant NAG5-9406 at the University of Michigan. G. Tóth is partially supported by the Education Ministry of Hungary (grant FKFP-0242-2000). M. Opher's research was performed at the Jet Propulsion Laboratory of the California Institute of Technology under a contract with NASA.

[53] Shadia Rifai Habbal thanks both referees for their assistance in evaluating this paper.

References

Aly, J. J. (1991), How much energy can be stored in a three-dimensional force-free magnetic field?, *Astrophys. J. Lett.*, *375*, L61–L64.

Amari, T., J. F. Luciani, Z. Mikić, and J. Linker (2000), A twisted flux rope model for coronal mass ejections and two-ribbon flares, *Astrophys. J. Lett.*, *529*, L49–L52.

Antiochos, S. K., C. R. DeVore, and J. A. Klimchuk (1999), A model for solar coronal mass ejections, *Astrophys. J.*, *510*, 485–493.

Axford, W. I., and J. F. McKenzie (1996), The acceleration of the solar wind, in *Solar Wind Eight*, edited by D. Winterhalter et al., *AIP Conf. Proc. Ser. 382*, 72–75.

Billings, D. W. (1966), *A Guide to the Solar Corona*, Academic, San Diego, Calif.

Chen, J. (1996), Theory of prominence eruption and propagation: Interplanetary consequences, *J. Geophys. Res.*, *101*, 27,499.

Chen, P. F., and K. Shibata (2000), An emerging flux trigger mechanism for coronal mass ejections, *Astrophys. J.*, *545*, 524–531.

Choe, G. S., and L. C. Lee (1996), Evolution of solar magnetic arcades. II. Effects of resistivity and solar eruptive processes, *Astrophys. J.*, *472*, 372–388.

DeSterck, H., B. C. Low, and S. Poedts (1998), Complex magnetohydrodynamic bow shock topology in field-aligned low-β flow around a perfectly conducting cylinder, *Phys. Plasmas*, *6*, 4015–4027.

Dryer, M., S. Wu, R. S. Steinolfson, and R. M. Wilson (1979), Magnetohydrodynamic models of coronal transients in the meridional plan. II. Simulation of the coronal transient of 1973 August 21, *Astrophys J.*, *227*, 1059.

Fan, Y., and B. C. Low (2003), Dynamics of CME driven by a BuoyantProminence flux tube, in *Proceedings of the 21st International NSO/SacPeak Workshop*, *ASP Conf. Ser.*, vol. 286, edited by A. A. Pevtsov and H. Uitenbroek, p. 347, Astron. Soc. of the Pacific, San Fransisco, Calif..

Fisk, L. A., N. A. Schwadron, and T. H. Zurbuchen (1999), Acceleration of the fast solar wind by the emergence of new magnetic flux, *J. Geophys. Res.*, *104*, 19,765–19,772.

Forbes, T. G. (2000), A review on the genesis of coronal mass ejections, *J. Geophys. Res.*, *105*, 23,153–23,165.

Forbes, T. G., and E. R. Priest (1995), Photospheric magnetic field evolution and eruptive flares, *Astrophys. J.*, *446*, 377–389.

Gibson, S., and B. C. Low (1998), A time-dependent three-dimensional magnetohydrodynamic model of the coronal mass ejection, *Astrophys. J.*, *493*, 460–473.

Groth, C. P. T., D. L. De Zeeuw, T. I. Gombosi, and K. G. Powell (2000), Global three-dimensional MHD simulation of a space weather event: CME formation, interplanetary propagation, and interaction with the magnetosphere, *J. Geophys. Res.*, *105*, 25,053–25,078.

Hollweg, J. V., S. Jackson, and D. Galloway (1982), Alfvén waves in the solar atmosphere. III. Nonlinear waves on open flux tubes, *Sol. Phys.*, *75*, 35–61.

Howard, R. A., et al. (1997), Observations of CMEs from SOHO/LASCO, in *Coronal Mass Ejections*, *Geophys Monogr. Ser.*, vol. 99, edited by N. Crooker, J. A. Joselyn, and J. Feynman, pp. 17–26, AGU, Washington, D. C.

Hundhausen, A. J. (1988), The origin and propagation of coronal mass ejections, in *Solar Wind Six*, edited by V. J. Pizzo, T. E. Holzer, and D. G. Sime, *Tech. Note NCAR/TN-306+Proc*, pp. 181–214, Natl. Cent. for Atmos. Res., Boulder, Colo.

Hundhausen, A. J. (1990), Coronal Mass Ejections: A summary of SMM observations from 1980 and 1984–1989, in *The Many Faces of the Sun*, edited by K. Strong, J. Saba, and B. Haisch, pp. 143–200, Springer-Verlag, New York.

Hundhausen, A. J. (1993), Sizes and locations of coronal mass ejections: SMM observations from 1980 and 1984–1989, *J. Geophys Res.*, *98*, 13,177–13,200.

Kabin, K. (2001), A note on the compression ratio in MHD shocks, *J. Plasma Phys.*, *66*, 259–274.

Leroy, J. L., V. Bommier, and S. Sahal-Brechot (1983), The magnetic field in the prominences of the polar crown, *Sol. Phys.*, *83*, 135–142.

Lin, J., and T. G. Forbes (2000), Effects of reconnection on the coronal mass ejection process, *J. Geophys. Res.*, *105*, 2375–2392.

Linker, J. A., and Z. Mikić (1995), Disruption of a helmet streamer by photospheric shear, *Astrophys. J. Lett.*, *438*, L45–L48.

Linker, J. A., Z. Mikić, R. Lionello, P. Riley, T. Amari, and D. Odstrcil (2003), Flux cancellation and coronal mass ejections, *Phys. Plasmas*, *10*, 1971–1978.

Low, B. C. (1983), Expolsion of magnetized plasmas from coronae, in *Solar and Stellar Magnetic Fields*: *Origins and Coronal Effects*, pp. 467–471, D., Reidel, Norwell, Mass.

Low, B. C. (1994), Magnetohydrodynamic processes in the solar corona: Flares, coronal mass ejections, and magnetic helicity, *Phys. Plasmas*, *1*, 1684–1690.

Low, B. C. (1996), Solar activity and the corona, *Sol. Phys.*, *167*, 217–265.

Low, B. C. (2001), Coronal mass ejections, magnetic flux ropes, and solar magnetism, *J. Geophys. Res.*, *106*, 25,141–25,163.

Low, B. C., and J. R. Hundhausen (1995), Magnetostatic structures of the solar corona. II. the magnetic topology of quiescent prominences, *Astrophys. J.*, *443*, 818–836.

Mancuso, S., J. C. Raymond, J. Kohl, Y.-K. Ko, M. Uzzo, and R. Wu (2002), UVCS/SOHO observations of a CME-driven shock: Consequences on ion heating mechanisms behind a coronal shock, *Astron. Astrophys.*, *383*, 267–274.

Mouschovias, T. C., and A. I. Poland (1978), Expansion and broadening of coronal loop transients: A theoretical explanation, *Astrophys. J.*, *220*, 675–682.

Mikić, Z., and J. A. Linker (1994), Disruption of coronal magnetic field arcades, *Astrophys. J.*, *430*, 898–912.

Mikić, Z., D. C. Barnes, and D. Schnack (1988), Dynamical evolution of a solar coronal magnetic field arcade, *Astrophys. J.*, *328*, 830–847.

Moore, R. L., A. C. Sterling, H. S. Hudson, and R. J. Lemen (2001), Onset of the magnetic explosions in solar flares and coronal mass ejections, *Astrophys J.*, *552*, 833.

Odstrcil, D., and V. J. Pizzo (1999), Three-dimensional propagation of coronal mass ejections (CMEs) in a structured solar wind flow: 1. CME launched within the streamer belt, *J. Geophys. Res.*, *104*, 483–492.

Odstrcil, D., M. Dryer, and Z. Smith (1996), Propagation of an interplanetary shock along the heliosphere plasma sheet, *J. Geophys. Res.*, *101*, 19,973–19,986.

Parker, E. N. (1963), *Interplanetary Dynamical Processes*, Wiley-Interscience, New York.

Pneuman, G. W., and R. A. Kopp (1971), Gas-magnetic field interactions in the solar corona, *Sol. Phys.*, *18*, 258–270.

Powell, K. G., P. L. Roe, T. J. Linde, T. I. Gombosi, and D. L. De Zeeuw (1999), A solution-adaptive upwind scheme for ideal magnetohydrodynamics, *J. Comput. Phys.*, *154*, 284.

Raymond, J. C., B. J. Thompson, O. C. St.Cyr, N. Gopalswamy, S. Kahler, M. Kaiser, A. Lara, A. Ciaravella, M. Romoli, and R. ONeal (2000), SOHO and radio observations of a CME shock wave, *Geophys. Res. Lett.*, *27*, 1439–1442.

Riley, P., J. A. Linker, Z. Mikić, D. Odstrcil, V. J. Pizzo, and D. F. Webb (2002), Evidence of posteruption reconnection associated with coronal mass ejections in the solar wind, *Astrophys. J.*, *578*, 972–978.

Sheeley, N. R., J. H. Walters, Y.-M. Wang, and R. A. Howard (1999), Continuous tracking of coronal outflows: Two kinds of coronal mass ejections, *J. Geophys Res.*, *104*, 24,739–24,767.

Sime, D. G., and A. J. Hundhausen (1987), The coronal mass ejection of July 6, 1980: A candidate for interpretation as a coronal shock wave, *J. Geophys Res.*, *92*, 1049–1055.

Steinolfson, R. S. (1991), Coronal evolution due to shear motion, *Astrophys. J.*, *382*, 677.

Steinolfson, R. S., and A. J. Hundhausen (1990), MHD intermediate shocks in coronal mass ejections, *J. Geophys. Res.*, *95*, 6389–6401.

Sterling, A. C., and H. S. Hudson (1997), X-ray dimming in halo coronal mass ejections, *Astrophys. J. Lett.*, *491*, L55.

Sturrock, P. A. (1991), Maximum energy of semi-infinite magnetic field configurations, *Astrophys. J.*, *380*, 655.

Tokman, M., and P. M. Bellan (2002), Three-dimensional model of the structure and evolution of coronal mass ejections, *Astrophys. J.*, *567*, 1202–1210.

Usmanov, A. V., M. L. Goldstein, B. P. Besser, and J. M. Fritzer (2000), A global MHD solar wind model with WKB Alfvén waves: Comparison with Ulysses data, *J. Geophys. Res.*, *105*, 12,675–12,696.

Vourlidas, A., P. Subramanian, K. P. Dere, and R. A. Howard (2000), Large-angle spectrometric coronagraph measurements of the energetics of coronal mass ejections, *Astrophys. J.*, *534*, 456–467.

Wang, Y.-M., and N. R. Sheeley Jr. (1994), Global evolution of the interplanetary sector structure, coronal holes, and solar wind streams during 1976–1993: Stackplot displays based on magnetic observations, *J. Geophys. Res.*, *99*, 6597–6608.

Wolfson, R. (1982), Equilibria and stability of coronal magnetic arcades, *Astrophys. J.*, *255*, 774.

Wu, S. T., and W. P. Guo (1997), A self-consistent numerical magnetohydrodynamic (MHD) model of helmet streamer and flux-rope interactions: Initiation and propagation of Coronal Mass Ejections (CMEs), in *Coronal Mass Ejections*, *Geophys. Monogr. Ser.*, vol. 99, edited by N. Crooker, J. A. Joselyn, and J. Feynman, pp. 83–89, AGU, Washington, D. C.

Wu, S. T., W. P. Guo, D. J. Michels, and L. F. Burlaga (1999), MHD description of the dynamical relationships between a flux rope, streamer, coronal mass ejection, and magnetic cloud: An analysis of the January 1997 Sun-Earth connection event, *J. Geophys. Res.*, *104*, 14,789–14,801.

Wu, S. T., W. P. Guo, S. P. Plunkett, B. Schmieder, and G. M. Simnett (2000), Coronal mass ejections (CMEs) initiation: Models and observations, *J. Atmos. Sol. Terr. Phys.*, *62*, 1489–1498.

Zhang, M., L. Golub, E. DeLuca, and J. Burkepile (2002), The timing of flares associated with the two dynamical types of coronal mass ejections, *Astrophys. J. Lett.*, *574*, L97–L100.

W. B. Manchester IV, T. I. Gombosi, I. Roussev, D. L. De Zeeuw, I. V. Sokolov, and K. G. Powell, Center for Space Environment Modeling, University of Michigan, 2455 Hayward Street, Ann Arbor, MI 48109, USA. (chipm@umich.edu; tamas@umich.edu; iroussev@umich.edu; darrens@umich.edu; igorsok@umich.edu; powell@engin.umich.edu)

G. Tóth, Department of Atomic Physics, Eotvos University, Pazmany setany 1/A, Budapest 1117, Hungary. (gtoth@hermes.elte.hu)

M. Opher, Jet Propulsion Laboratory, California Institute of Technology, Pasadena, CA 91109-8099, USA. (merav.opher@jpl.nasa.gov)